Key Engineering Materials
ISSN: 1662-9795, Vol. 926, pp 917-925
doi:10.4028/p-dds916

Submitted: 2021-12-06
Revised: 2022-01-11
Accepted: 2022-02-04
Online: 2022-07-22

Local Formability of Different Advanced High Strength Steels

Fuhui Shen[1,a*], Hesong Wang[1,b**], Hao Xu[1,c], Wenqi Liu[2,d], Sebastian Münstermann[1,e] and Junhe Lian[2,f]

[1]Integrity of Materials and Structures, Steel Institute, RWTH Aachen University, Intzestraße 1, 52072 Aachen, Germany

[2]Advanced Manufacturing and Materials, Department of Mechanical Engineering, Aalto University, Puumiehenkuja 3, 02150 Espoo, Finland

Corresponding author: [a]fuhui.shen@iehk.rwth-aachen.de, [b]wanghesongsy@hotmail.com, [c]hao.xu@iehk.rwth-aachen.de, [d]wenqi.liu@aalto.fi, [e]Sebastian.Muenstermann@iehk.rwth-aachen.de, [f]junhe.lian@aalto.fi

Keywords: Forming limits; Damage mechanics; Medium-Mn steels; Stress state

Abstract. Medium-Mn steel (MMnS) is a promising candidate of the third generation of advanced high strength steels (AHSS), which can provide superior tensile properties. To consider the edge crack issues, the local formability, as an indicator of fracture resistance, of the MMnS needs to be quantitatively evaluated for their potential application to industries. Thus, the local formability of two different MMnS is evaluated by the forming limits at fracture using the damage mechanics approaches and compared with a DP1000 steel in this study. Despite the superior tensile properties, the local formability of the investigated MMnS is worse than the DP1000, which is characterized by the fracture strain under different stress states. Therefore, for the assessment of their potential application in automotive industries, it is recommended that more attention should be paid to the local formability and fracture resistance of these advanced high strength steels.

Introduction

The application of advanced high strength steels (AHSSs) is one of the most effective ways to meet the urgent demands on weight reduction and improved crashworthiness property in the modern automotive industry. In recent years, medium-Mn steels (4–12 wt.% Mn) have received significant attention as a promising representative of the third-generation AHSSs because of the excellent combination of strength and ductility together with suitable materials cost [1, 2]. Superior tensile properties, i.e., high strength, high ductility, pronounced strain hardening capacity, are reasonable indicators of excellent global formability, which is typically characterized by the forming limits at necking. However, ductile fracture occurs with slight or even no necking in some AHSS and edge cracking is often observed in the forming processes of different AHSS [3, 4]. Therefore, the local formability is a critical material property that needs to be considered for the assessment of edge crack sensitivity [5, 6].

The local formability is an indicator of fracture resistance, which is particularly important for forming processes with concentrated plastic deformation. The local formability can be evaluated using the hole expansion tests or bending tests [7]. Alternatively, the fracture strains determined in different stress states are also efficient parameters to evaluate the local formability of metallic materials [8, 9]. The tendency of edge cracking, due to pre-damage effects in the edge area accumulated from previous shearing forming operations, is reduced in materials with higher fracture strains and improved local formability. To determine the fracture strains over a broad range of stress states, the uncoupled damage mechanics approach has been widely applied for many different metallic materials due to the advantages of simple formulation and easy parameter calibration procedures [10, 11]. The failure strain is typically formulated as a weight function of stress state variables, i.e., stress triaxiality and Lode angle parameter, in the family of recently developed uncoupled damage mechanics models, including the Bai–Wierzbicki (BW) model [12], modified Mohr–Coulomb (MMC) model [13], modified Hosford–Coulomb (MHC) model [14], and the series

of ductile fracture models proposed by Lou et al. [15]. The hybrid modified Bai–Wierzbicki (MBW) model presented by Lian et al. [16] has also been frequently used to depict damage and fracture phenomena of various types of steels under different loading conditions [17].

The local formability of the first generation of AHSS, mainly DP steels and TRIP steels, has been investigated in many studies [13, 14, 18]. There are also several investigations on the local formability of TWIP steels, representatives of the second generation of AHSS, where ductile fracture instead of localization is the main failure pattern [4, 19]. However, the local formability of the third generation AHSS has not been fully exploited. In the present study, the local formability of two medium-Mn steels (MMnS) produced by different processes has been determined by performing tensile tests using flat specimens with various notch configurations. Based on finite element simulations using the damage mechanics approaches, the local formability, quantified by the forming limits at fracture, of these MMnS is evaluated and compared with a DP1000 steel.

Material Characterization and Experiments

Materials. The local formability of two different medium-Mn steels, one hot-rolled (MMnS-H) and one cold-rolled (MMnS-C), is compared with a dual-phase DP1000 steel. The MMnS steel billet was austenitized at 1200 °C for 1.5 h, followed by hot rolling and intercritical annealing at 720 °C for 30 min. The intercritically annealed hot-rolled MMnS was further subjected to cold rolling and intercritical annealing at 720 °C for 20 min. The schematic diagram of the processing route is presented in Fig. 1.

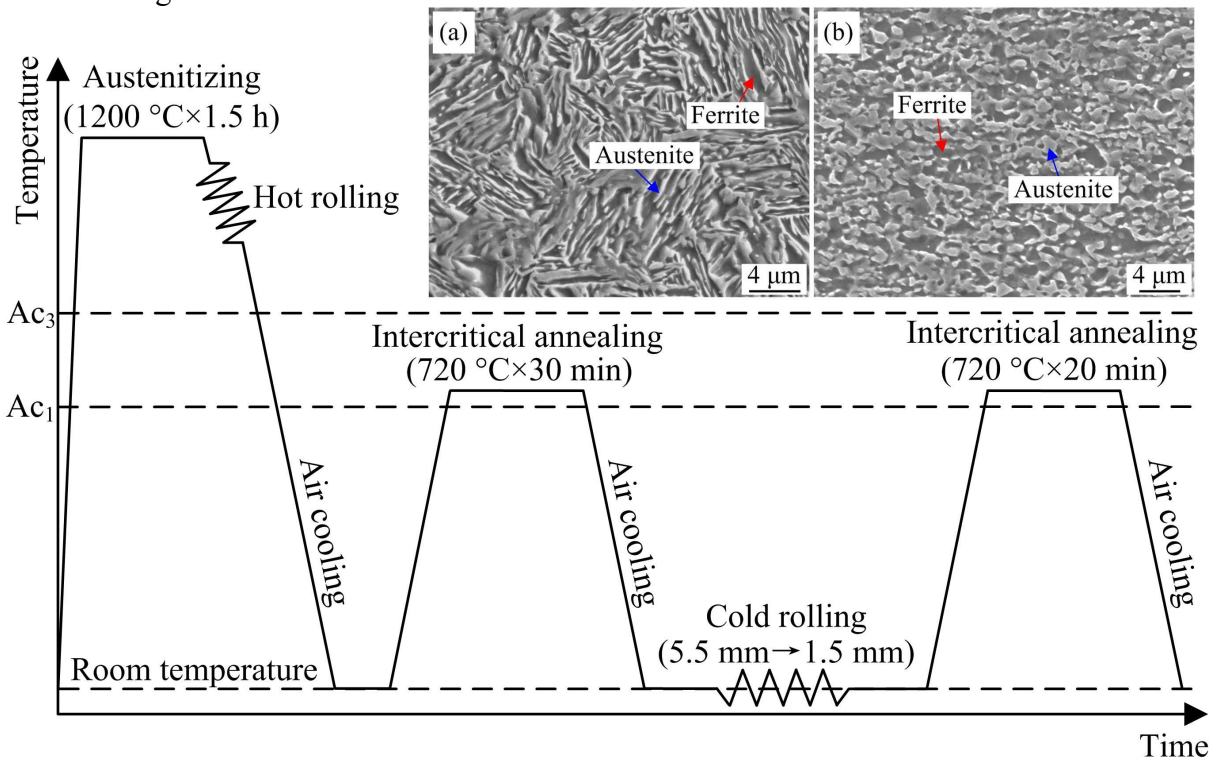

Figure 1. Schematic diagram of the processing route and microstructure of the medium-Mn steel (MMnS): (a) hot-rolled MMnS (MMnS-H) after intercritical annealing and (b) cold-rolled MMnS (MMnS-C) after intercritical annealing.

Due to the different heat treatments, the microstructures of hot-rolled MMnS-H and cold-rolled MMnS-C are different, as shown in Fig. 1. Lath ferrite and lath austenite are present in the hot-rolled MMnS-H steel because of the austenite reverted transformation (Fig. 1a). Typical globular ferrite and globular austenite are obtained in the cold-rolled MMnS-C steel (Fig. 1b), and the volume fraction of austenite is ~ 45%. The microstructure of the DP1000 steel consists of ferrite and martensite (~ 45 % volume fraction).

Mechanical tests. For the characterization of the plastic flow behavior of different steels at room temperature, uniaxial tensile tests have been performed using smooth dog-bone (SDB) specimens according to DIN EN ISO 6892-1. Uniaxial tensile properties of two representative MMnS produced by different processes are compared with a DP1000 steel, which has similar yield strength, as shown in Fig. 2. Serrated flow behavior is observed in both hot-rolled and cold-rolled MMnS, which is due to the dynamic strain aging mechanisms in MMnS. Due to the difference in the microstructure, a Lüders strain is observed in the cold-rolled MMnS-C. Despite the fact that a certain degree of heterogeneity occurs in the deformation of both MMnS before reaching the ultimate tensile strength, it is evident that the engineering global uniform elongation and fracture elongation of both MMnS are larger than the DP1000. There is a post-necking deformation stage in the DP1000 steel, while fracture occurs almost immediately after reaching the ultimate tensile strength in both MMnS. In general, it is observed that both MMnS have superior tensile properties than DP1000 in terms of their high ductility and pronounced strain hardening capacity.

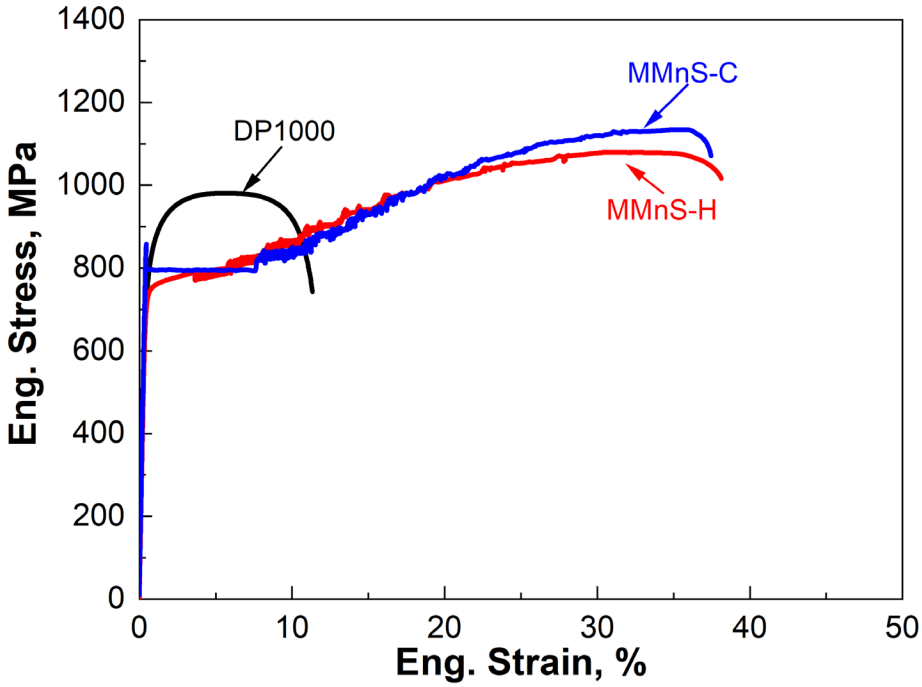

Figure 2. Uniaxial tensile stress and strain curves of two different medium-Mn steels (MMnS-H and MMnS-C) and DP1000 steel.

Local formability is considered as the ductile fracture resistance in this study. Therefore, the ductile fracture behavior of these three advanced high strength steels is characterized under different stress states. Tensile tests using flat specimens with various geometries have been performed to analyze the effects of stress states on the ductile fracture properties of the investigated material at room temperature. The dimensions of the tested samples are summarized in Fig. 3, including one shear (SH) geometry, one central hole (CH-R3) geometry and two side-grooved plane strain (PS-R16, PS-R2) geometries. The thickness of all tensile specimens is 1.5 mm. The broad range of stress states between shear and plane strain tension can be covered by the designed testing program. All tensile tests have been conducted under quasi-static loading conditions. Detailed experimental procedures are explained in [9]. As shown in Fig. 3, there is a difference in the sample dimensions used for different materials. The same specimen geometries (width of 20 mm in the critical region) are used for the DP1000 and the hot-rolled MMnS-H. The width of tensile specimens is smaller for the cold-rolled MMnS-C due to the shortage of available material. Both categories of tensile geometries have been verified to provide desired stress states in the critical region. Therefore, the slight geometrical difference does not have impacts on the final results.

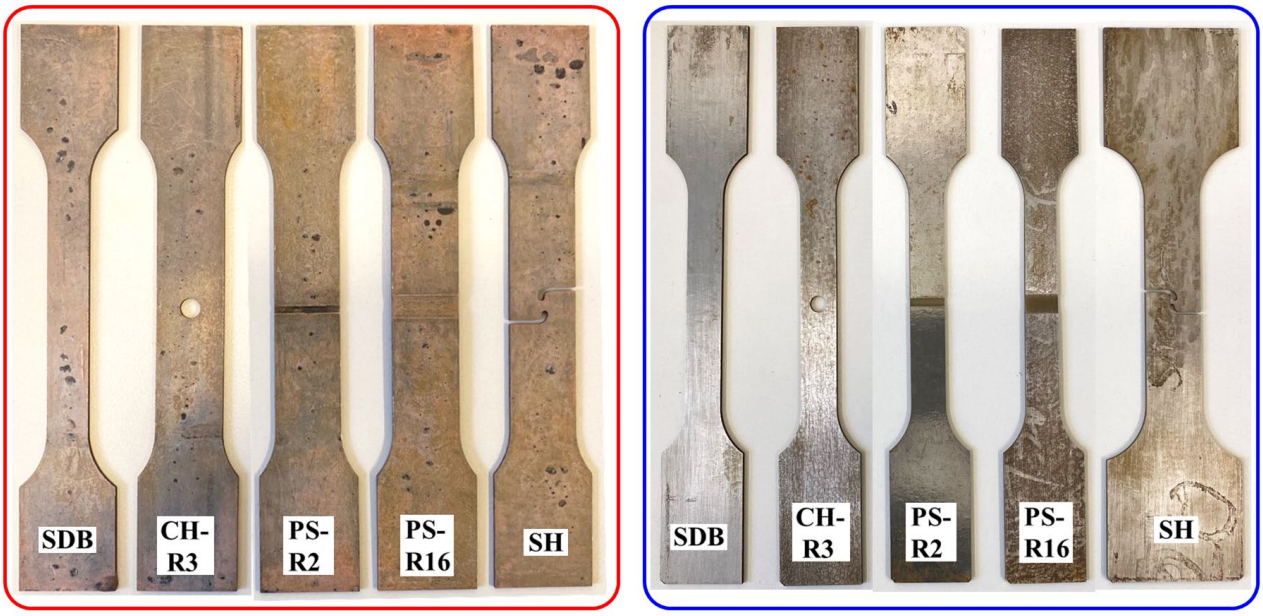

Figure 3. Overview of the geometry of plasticity and fracture specimens: (left) DP1000 and MMnS-H and (right) MMnS-C.

Damage Mechanics Models

A hybrid phenomenological damage mechanics model, which is modified from the original Bai–Wierzbicki (MBW) model by Lian et al. [16], has been used to describe the deformation and ductile fracture behavior of different advanced high strength steels in this study. Detailed derivation and annotation of the MBW model could be found in [9, 20]. The effects of stress states on the failure properties of isotropic materials are determined by the two most widely applied variables [18], i.e., the triaxiality η and the Lode angle parameter $\overline{\theta}$, which can be derived from three stress invariants (I_1, J_2, J_3).

$$\eta = \frac{I_1}{3\sqrt{3 \cdot J_2}} = \frac{(\sigma_1+\sigma_2+\sigma_3)}{3\sqrt{\frac{1}{2}[(\sigma_1-\sigma_2)^2+(\sigma_2-\sigma_3)^2+(\sigma_3-\sigma_1)^2]}}. \tag{1}$$

$$\overline{\theta} = 1 - \frac{2}{\pi}\cos^{-1}\left(\frac{3\sqrt{3}}{2}\frac{J_3}{J_2^{3/2}}\right). \tag{2}$$

Under plane stress conditions, these two stress state variables (η, $\overline{\theta}$) can be converted from each other.

$$\cos\left[\frac{\pi}{2}(1-\overline{\theta})\right] = -\frac{27}{2}\eta\left(\eta^2 - \frac{1}{3}\right). \tag{3}$$

When neglecting the effects of triaxiality and Lode angle parameter on plasticity, the isotropic Mises equivalent stress $\bar{\sigma}(\boldsymbol{\sigma})$ is applied in the yield criterion f and a scalar damage variable D is used to quantify the damage effects. The normality flow rule is used in this study. The flow stress $\sigma_y(\overline{\varepsilon}^p)$ is described using the combined Swift-Voce hardening law for these materials.

$$f = \bar{\sigma}(\boldsymbol{\sigma}) - (1-D)\sigma_y(\overline{\varepsilon}^p) \leq 0. \tag{4}$$

$$\bar{\sigma}(\boldsymbol{\sigma}) = \sqrt{\frac{1}{2}[(\sigma_1-\sigma_2)^2 + (\sigma_2-\sigma_3)^2 + (\sigma_3-\sigma_1)^2]}. \tag{5}$$

$$\sigma_y(\overline{\varepsilon}^p) = \alpha \cdot A \cdot (\bar{\varepsilon}^p + \varepsilon_0)^n + (1-\alpha)\cdot\left[k_0 + Q\cdot(1-exp^{-\beta\cdot\bar{\varepsilon}^p})\right]. \tag{6}$$

In order to consider the effects of stress state evolution during plastic deformation, the average stress triaxiality η_{avg} and average Lode angle parameter $\overline{\theta}_{\mathrm{avg}}$ are used to characterize the overall stress states for each geometry. A ductile damage initiation locus is defined by the critical equivalent plastic strain $\overline{\varepsilon}^{\mathrm{p}}_{\mathrm{di}}$ as a function of stress state parameters. A ductile damage indicator I_{dd} is used to describe the accumulation degree of damage under non-proportional loading conditions. The ductile fracture occurs once the indicator I_{dd} reaches unity during plastic deformation.

$$\overline{\varepsilon}^{\mathrm{p}}_{\mathrm{di}}\left(\eta_{\mathrm{avg}},\overline{\theta}_{\mathrm{avg}}\right)=\left[D_1 exp^{-D_2\eta_{\mathrm{avg}}}-D_3 exp^{-D_4\eta_{\mathrm{avg}}}\right]\overline{\theta}_{\mathrm{avg}}{}^{2}+D_3 exp^{-D_4\eta_{\mathrm{avg}}}. \tag{7}$$

$$I_{\mathrm{dd}}=\int_0^{\overline{\varepsilon}^{\mathrm{p}}}\frac{d\overline{\varepsilon}^{\mathrm{p}}}{\overline{\varepsilon}^{\mathrm{p}}_{\mathrm{di}}(\eta_{\mathrm{avg}},\overline{\theta}_{\mathrm{avg}})}. \tag{8}$$

Simulation Results

Calibration and validation of model parameters. Tensile deformation of different specimens has been simulated for each material using the finite element method. To simulate the crack initiation and propagation, the element deletion approach has been adopted using the ABAQUS/Explicit software. Half-thickness finite element models with the solid element type have been created and a fine mesh of 0.1×0.1×0.1 mm^3 has been used in the critical region of different tensile geometries. The calibrated strain hardening parameters in the combined Swift-Voce hardening law are summarized in Table 1 for three different advanced high strength steels.

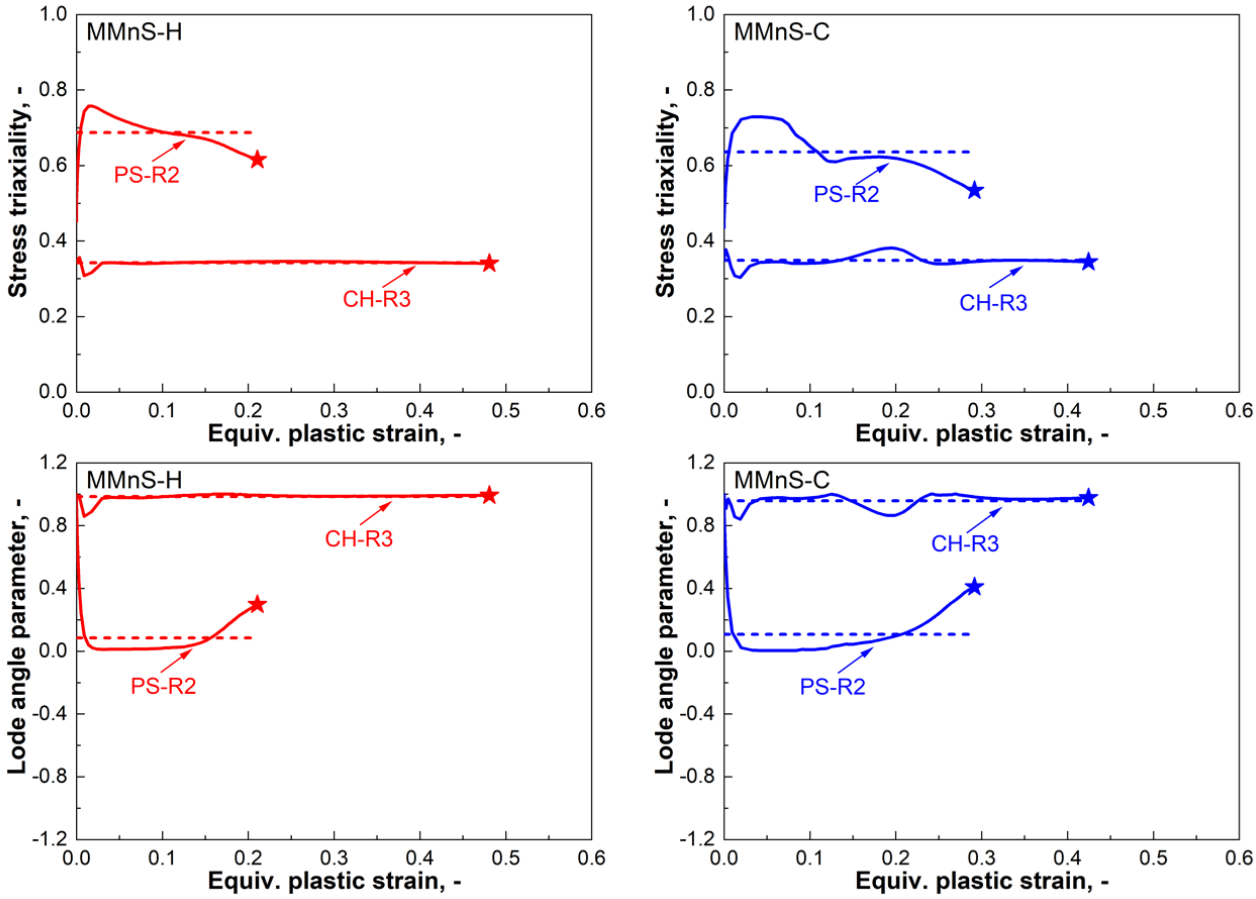

Figure 4. Evolution of local stress triaxiality and Lode angle parameter in critical elements during tensile deformation of the central hole (CH-R3) and plane strain (PS-R2) specimens in two different medium-Mn steels: (left) MMnS-H and (right) MMnS-C.

Based on the finite element simulation results using the calibrated plasticity model, the evolution of local stress states (stress triaxiality and Lode angle parameter) with equivalent plastic strain in the critical elements of different specimens has been collected. In Fig. 4, the evolution of local stress triaxiality and Lode angle parameter (solid curves) until the fracture initiation (star symbols) is demonstrated for tensile deformation of the central hole (CH-R3) and plane strain (PS-R2) specimens of two different MMnS. The average values of stress triaxiality and Lode angle parameter are represented by dashed curves.

Table 1 Calibrated hardening parameters of two different medium-Mn steels (MMnS-H and MMnS-C) and DP1000 steel.

Material	$\sigma = \alpha \cdot A \cdot (\bar{\varepsilon}^{\mathrm{p}} + \varepsilon_0)^n + (1-\alpha) \cdot \left[k_0 + Q \cdot (1 - exp^{-\beta \cdot \bar{\varepsilon}^{\mathrm{p}}})\right]$						
	A	ε_0	n	α	k_0	Q	β
MMnS-H	2720.00	0.21	0.866	0.00	640.60	2400.00	1.56
MMnS-C	3267.00	0.30	1.324	1.00	538.50	2000.00	2.358
DP1000	1300.00	0.00	0.075	0.50	773.28	266.19	73.94

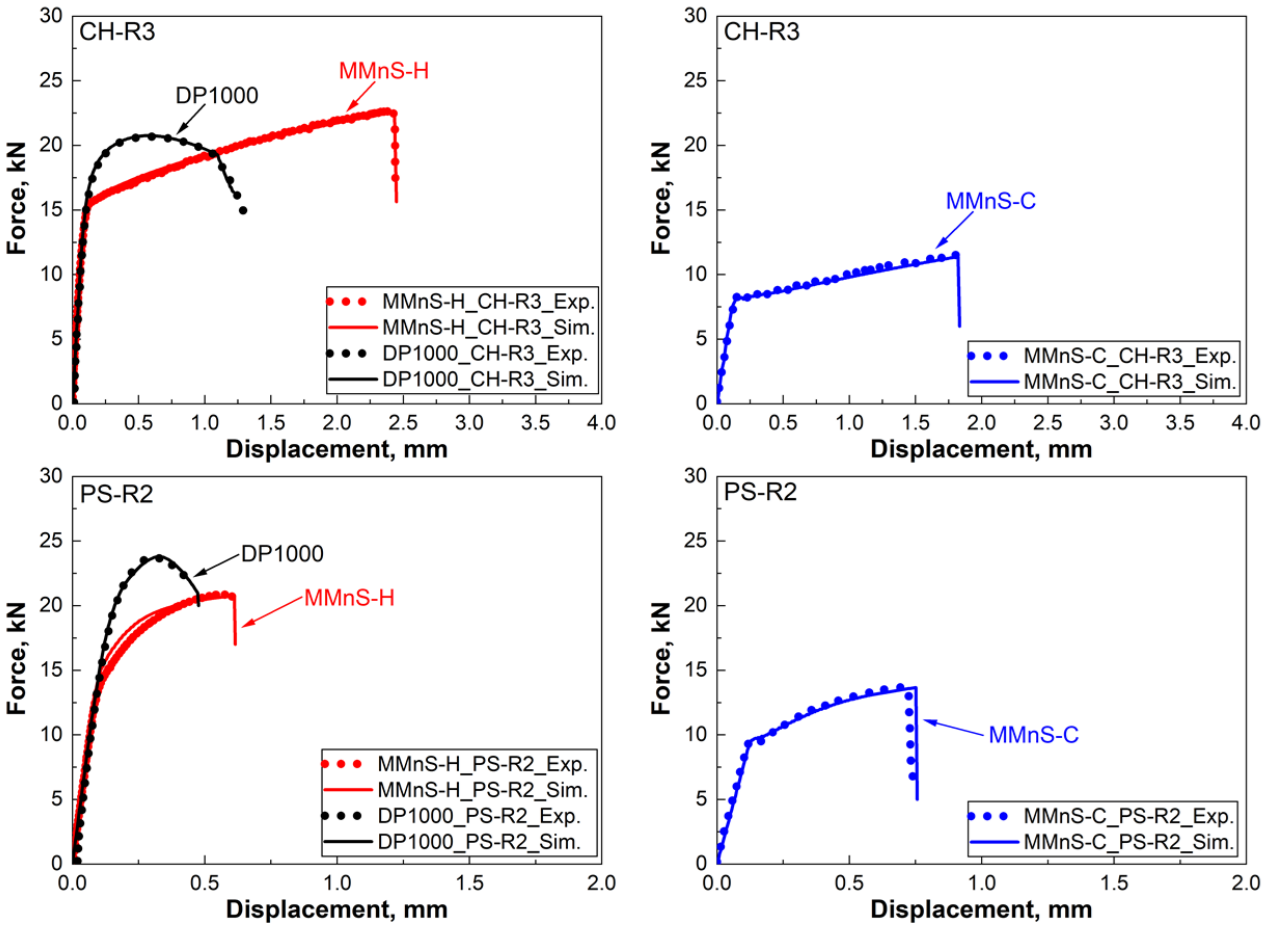

Figure 5. Prediction of ductile fracture in tensile tests of the central hole (CH-R3) and plane strain (PS-R2) specimens in different advanced high strength steels: (left) DP1000 and MMnS-H and (right) MMnS-C.

At the fracture displacements of different tensile geometries, the local strain and stress variables, including equivalent plastic strain, stress triaxiality and Lode angle parameter, are taken from the critical elements based on the finite element simulation results. Given the equivalent plastic strain and stress state variables at the fracture point collected from tensile tests using different sample geometries, an optimization algorithm is applied to determine the ductile damage initiation locus

parameters for each material. With the calibrated damage parameters for individual advanced high strength steels, the tensile displacements at fracture in tensile tests can be accurately predicted, as shown in Fig. 5. The simulation results of the central hole (CH-R3) and plane strain (PS-R2) specimens are shown in Fig. 5. It is noticed that the displacements at fracture of the MMnS-H are larger than DP1000 in both the CH-R3 and PS-R2 geometries, when identical sample geometries are used for both materials. The distribution of equivalent plastic strain at fracture displacements of the central hole (CH-R3) specimens is represented in Fig. 6 on the mid-thickness plane and two perpendicular cross-sections. As shown in Fig. 5, the displacement at fracture of the CH-R3 geometry is 2.5 mm for the MMnS-H and 1.1 mm for the DP1000, respectively. However, it is noticed that the maximum value of equivalent plastic strain is smaller in the MMnS-H than the DP1000 even a larger global tensile displacement is applied to the MMnS-H specimen. The plastic deformation is distributed more homogeneously in the MMnS due to the pronounced hardening capacity, which provides an excellent global formability and necking resistance. These results indicate the MMnS-H can sustain larger global plastic deformation than the DP1000.

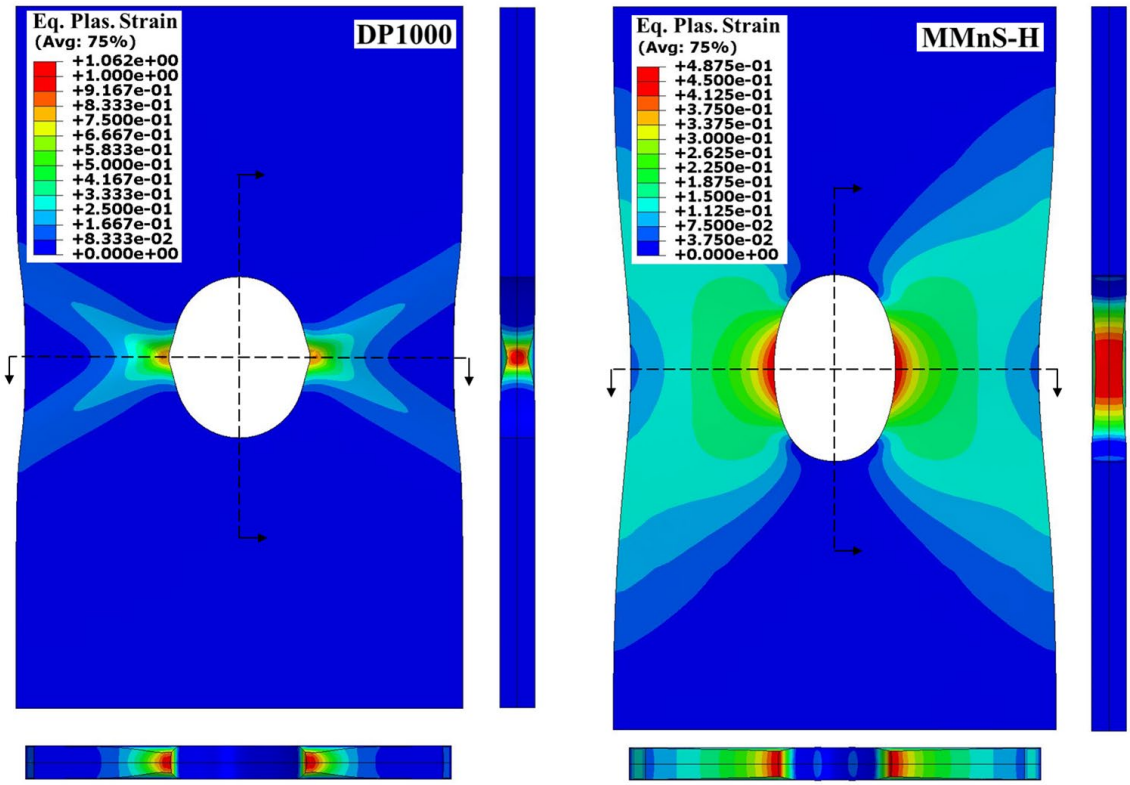

Figure 6. Distribution of the equivalent plastic strain at fracture displacements on the mid-thickness plane in tensile tests of central hole (CH-R3) specimens for the MMnS-H and DP1000.

Comparison of local formability of different steels. Due to the limitation of space, only the local formability of these different AHSS is compared, which is an indicator of fracture resistance. The local formability needs to be evaluated under different stress states from shear to plane strain tension which is essential for relevant forming processes. The fracture strain is not directly measured from experiments but inversely determined based on finite element simulations of tensile tests using four geometries. For the quantitative comparison of the local formability of these AHSS, the equivalent plastic strain at fracture determined from simulation results is plotted over stress triaxiality in Fig. 7. The numerically determined results of fracture strain and stress triaxiality in these four tensile geometries are represented as solid symbols in Fig. 7. The solid curve, which is defined as the forming limit curve at fracture (FLC_f), is the determined damage initiation locus under plane stress conditions ($\boldsymbol{\sigma_2 = 0}$ or $\boldsymbol{\sigma_3 = 0}$), according to Eq. 3 and Eq. 8, for each material. It is noticed that the fracture strain values are similar in both MMnS produced by different processes, which are much lower than the fracture strain values of DP1000. When the fracture strain is used as the parameter to evaluate the

local formability, the local formability of two different medium-Mn steels is worse than the dual-phase DP1000, despite the superior tensile properties of MMnS. These results indicate a high risk of ductile fracture when the investigated MMnS is subjected to forming processes with highly localized plastic deformation. Therefore, it is recommended that more attention should be paid to the local formability and fracture resistance of the new generation of AHSS.

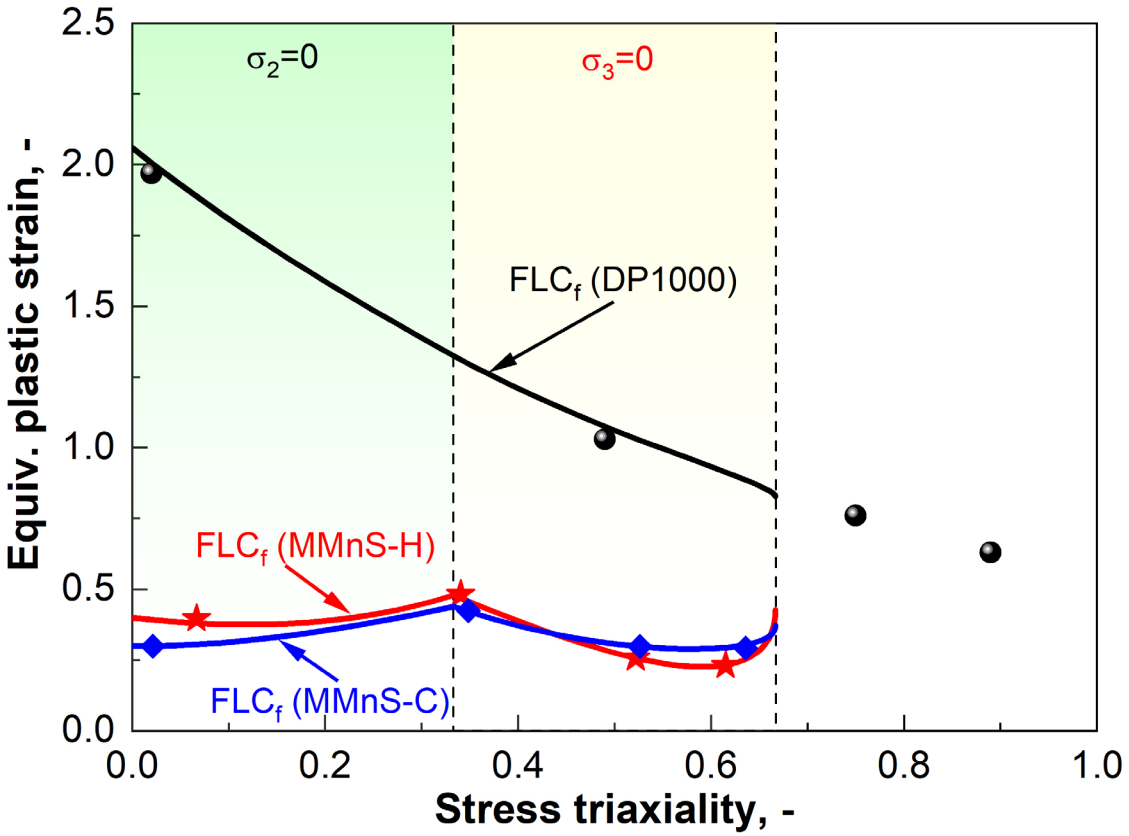

Figure 7. Comparison of the local formability of different advanced high strength steels: Symbols correspond to numerical results of four tensile geometries, and solid curves represent the continuous forming limit curve at fracture determined by the damage mechanics model.

Summary

By analyzing the uniaxial tensile properties and local formability of several different advanced high strength steels using damage mechanics approaches, the following conclusions are drawn:

- To assess the formability of advanced high strength steels, the local formability and global formability should be distinguished.
- A very good global formability against necking is expected in the investigated MMnS due to its superior tensile properties, in particular the pronounced hardening capacity.
- Despite the superior tensile properties, the local formability of the investigated MMnS produced by different processes is worse than a reference DP1000 steel with similar strength properties.

Acknowledgments

Hesong Wang acknowledges the China Scholarship Council (No. 201906080029) providing an opportunity to study in Aachen, Germany. Simulations were performed with computing resources granted by RWTH Aachen University under project < rwth0779 >.

References

[1] B. Hu, H. Luo, F. Yang, H. Dong, Recent progress in medium-Mn steels made with new designing strategies, a review, Journal of Materials Science & Technology 33(12) (2017) 1457-1464.
[2] J. Hu, L.-X. Du, W. Xu, J.-H. Zhai, Y. Dong, Y.-J. Liu, R.D.K. Misra, Ensuring combination of strength, ductility and toughness in medium-manganese steel through optimization of nano-scale metastable austenite, Materials Characterization 136 (2018) 20-28.
[3] Y. Li, M. Luo, J. Gerlach, T. Wierzbicki, Prediction of shear-induced fracture in sheet metal forming, Journal of Materials Processing Technology 210(14) (2010) 1858-1869.
[4] K. Chung, H. Kim, C. Lee, Forming limit criterion for ductile anisotropic sheets as a material property and its deformation path insensitivity. Part I: Deformation path insensitive formula based on theoretical models, International Journal of Plasticity 58 (2014) 3-34.
[5] S. Heibel, T. Dettinger, W. Nester, T. Clausmeyer, A.E. Tekkaya, Damage Mechanisms and Mechanical Properties of High-Strength Multiphase Steels, Materials (Basel) 11(5) (2018).
[6] B. Hance, Advanced high strength steel: Deciphering local and global formability, Proc. International Automotive Body Congress, Dearborn, MI, 2016.
[7] M. Kaupper, M. Merklein, Bendability of advanced high strength steels—A new evaluation procedure, CIRP Annals 62(1) (2013) 247-250.
[8] L. Mu, Z. Jia, Z. Ma, F. Shen, Y. Sun, Y. Zang, A theoretical prediction framework for the construction of a fracture forming limit curve accounting for fracture pattern transition, International Journal of Plasticity 129 (2020).
[9] F. Shen, H. Wang, Z. Liu, W. Liu, M. Könemann, G. Yuan, G. Wang, S. Münstermann, J. Lian, Local formability of medium-Mn steel, Journal of Materials Processing Technology 299 (2022).
[10] N. Park, H. Huh, S.J. Lim, Y. Lou, Y.S. Kang, M.H. Seo, Fracture-based forming limit criteria for anisotropic materials in sheet metal forming, International Journal of Plasticity 96 (2017) 1-35.
[11] C.C. Roth, D. Mohr, Determining the strain to fracture for simple shear for a wide range of sheet metals, International Journal of Mechanical Sciences 149 (2018) 224-240.
[12] Y. Bai, T. Wierzbicki, A new model of metal plasticity and fracture with pressure and Lode dependence, International Journal of Plasticity 24(6) (2008) 1071-1096.
[13] Y. Bai, T. Wierzbicki, Application of extended Mohr–Coulomb criterion to ductile fracture, International Journal of Fracture 161(1) (2009) 1-20.
[14] D. Mohr, S.J. Marcadet, Micromechanically-motivated phenomenological Hosford–Coulomb model for predicting ductile fracture initiation at low stress triaxialities, International Journal of Solids and Structures 67-68 (2015) 40-55.
[15] Y. Lou, L. Chen, T. Clausmeyer, A.E. Tekkaya, J.W. Yoon, Modeling of ductile fracture from shear to balanced biaxial tension for sheet metals, International Journal of Solids and Structures 112 (2017) 169-184.
[16] J. Lian, M. Sharaf, F. Archie, S. Münstermann, A hybrid approach for modelling of plasticity and failure behaviour of advanced high-strength steel sheets, International Journal of Damage Mechanics 22(2) (2012) 188-218.
[17] F. Shen, S. Münstermann, J. Lian, Investigation on the ductile fracture of high-strength pipeline steels using a partial anisotropic damage mechanics model, Engineering Fracture Mechanics 227 (2020) 106900.
[18] F. Pütz, F. Shen, M. Könemann, S. Münstermann, The differences of damage initiation and accumulation of DP steels: a numerical and experimental analysis, International Journal of Fracture 226(1) (2020) 1-15.
[19] M.C. Butuc, F. Barlat, G. Vincze, The formability of twinning—Induced plasticity steels predicted on the base of Marciniak-Kuczynski theory, Journal of Materials Processing Technology 287 (2021).
[20] W. Liu, J. Lian, S. Münstermann, C. Zeng, X. Fang, Prediction of crack formation in the progressive folding of square tubes during dynamic axial crushing, International Journal of Mechanical Sciences 176 (2020).